analytical chemistry

pubs.acs.org/ac Article

Toward Next-Generation Molecular Imaging with a Clinical Low-Field (0.064 T) Point-of-Care MRI Scanner

Nadiya Iqbal, Drew O. Brittin, Praveen J. Daluwathumullagamage, Md Shahabuddin Alam, Ishani M. Senanayake, A. Tobi Gafar, Zahid Siraj, Anthony Petrilla, Margaret Pugh, Brockton Tonazzi, Sudarshan Ragunathan, Megan E. Poorman, Laura Sacolick, Thomas Theis, Matthew S. Rosen, Eduard Y. Chekmenev, and Boyd M. Goodson*

Cite This: *Anal. Chem.* 2024, 96, 10348−10355 Read Online

ACCESS | Metrics & More | Article Recommendations | Supporting Information

ABSTRACT: Low-field (LF) MRI promises soft-tissue imaging without the expensive, immobile magnets of clinical scanners but generally suffers from limited detection sensitivity and contrast. The sensitivity boost provided by hyperpolarization can thus be highly synergistic with LF MRI. Initial efforts to integrate a continuous-bubbling SABRE (signal amplification by reversible exchange) hyperpolarization setup with a portable, point-of-care 64 mT clinical MRI scanner are reported. Results from ^{1}H SABRE MRI of pyrazine and nicotinamide are compared with those of benchtop NMR spectroscopy. Comparison with MRI signals from samples with known H_2O/D_2O ratios allowed quantification of the SABRE enhancements of imaged samples with various substrate concentrations (down to 3 mM). Respective limits of detection and quantification of 3.3 and 10.1 mM were determined with pyrazine ^{1}H polarization (P_H) enhancements of ∼1900 (P_H ∼0.04%), supporting ongoing and envisioned efforts to realize SABRE-enabled MRI-based molecular imaging.

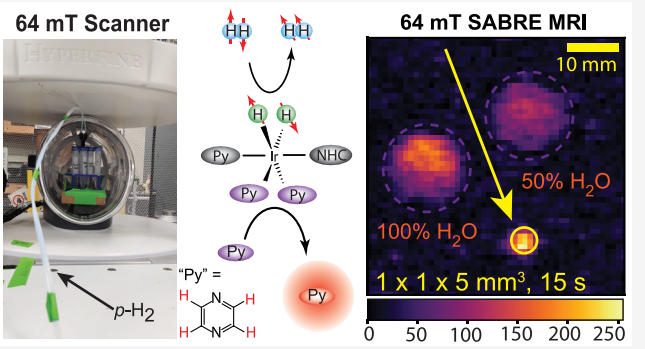

INTRODUCTION

MRI provides high-resolution images of anatomical features, function, and pathology of soft tissues in the body—without the need for ionizing radiation. However, the strong magnets used in most clinical scanners (∼1−7 T) are expensive, bulky, and immobile, and scans can be time-consuming and confining. Moreover, these strong magnetic fields can present safety concerns in some circumstances, as well as contra-indications for a number of health conditions. Low-field (LF) MRI[1−10] has gained renewed interest because it can obviate these limitations. However, insufficient signal strength, detection sensitivity, and contrast present ongoing challenges to many LF MRI technologies.

One approach to mitigate these shortcomings is hyperpolarization. Hyperpolarization involves the preparation of nuclear spin polarization levels that are far above their equilibrium values[11,12]—thereby increasing the detection sensitivity by orders of magnitude. Hyperpolarization can enable faster acquisition, greater signal, improved resolution, and the imaging of substances with lower concentrations. Moreover, because the nuclear spin magnetization is endowed by the hyperpolarization method and not by the magnet, the detection sensitivity of hyperpolarized (HP) LF MRI[9,13−16] can approach—and in some cases, even surpass—that of high-field MRI.[13] Thus, hyperpolarization can be highly synergistic with LF MRI, particularly if the hyperpolarization technique is itself low-cost, rapid, and portable.[14−16] One such approach is signal amplification by reversible exchange (SABRE).[17] In SABRE, parahydrogen (p-H_2) and a substrate are transiently bound to an organometallic complex, allowing spin order to transfer spontaneously from p-H_2 to the substrate when placed within an appropriate magnetic field. Indeed, the high speed and low instrumentation demands of SABRE make it well-suited for LF NMR and MRI.[14−16,18−21]

Here, we report on recent efforts to integrate SABRE with a portable, "point-of-care" 64 mT clinical MRI scanner (Figure 1). This type of scanner has already been demonstrated in clinical investigations for bedside imaging, including for brain injury and cerebral hemorrhage;[22,23] indeed, it has now received FDA approval for clinical use. Such scanners have also been used in fundamental studies to measure LF T_1/T_2 relaxation in human brain tissues[24] and to investigate using

Received: March 9, 2024
Revised: May 7, 2024
Accepted: May 22, 2024
Published: June 10, 2024

https://doi.org/10.1021/acs.analchem.4c01299
Anal. Chem. 2024, 96, 10348−10355

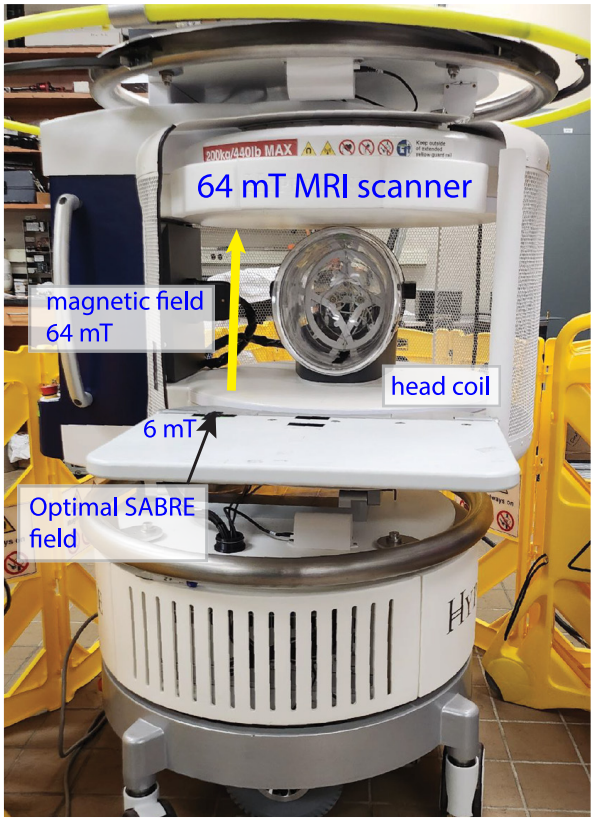

Figure 1. Portable point-of-care 64 mT clinical MRI scanner (Hyperfine "*Swoop*") used in this work.

superparamagnetic iron-oxide nanoparticles to generate positive contrast in LF MRI.[25] Here, target molecules of interest include pyrazine,[26] a prototypical nitrogen heterocycle with four magnetically equivalent ^{1}H sites, and nicotinamide (a.k.a. vitamin B_3-amide), a potential agent for hyperpolarized ^{1}H (and ^{15}N) biomedical MRI[27−31] with a low incidence of side effects and toxicity. SABRE-enhanced LF MR images were successfully acquired with both substrates under continuous *p*-H_2 bubbling or static conditions and compared with those of benchtop NMR spectroscopy. Comparison with MRI signals from water samples with known H_2O/D_2O ratios allowed the SABRE enhancements in the images to be quantified. Variation of the pyrazine substrate concentration (down to 3 mM) allowed the limit of detection (LOD) and limit of quantification (LOQ) of 3.3 and 10.1 mM to be respectively determined, with pyrazine ^{1}H polarization (P_H) enhancements of ∼1900 (P_H ∼0.04%). Taken together, these results comprise an important first step toward the development of sensitive and ultrafast point-of-care MRI with hyperpolarized agents.

MATERIALS AND METHODS

Pyrazine (Py), nicotinamide (nico), deuterated methanol, and deuterated water (99%) were purchased from Sigma-Aldrich and used without further purification (18 MΩ water was sourced in-house). An IrIMes(COD)Cl [IMes = 1,3-bis(2,4,6-trimethylphenyl), imidazole-2-ylidene; COD = cyclo-octa-diene] precatalyst[32−34] was used in all SABRE experiments and was synthesized and purified according to previous procedures.[35]

Seven 15 mL falcon tubes containing 10.00 mL of "0%", 10%, 25%, 50%, 75%, 90%, and 100% H_2O by volume (backfilled with D_2O) were used as the MR signal calibration standards. *p*-H_2 gas was provided by an ∼86% *p*-H_2 generator.[36] All SABRE experiments were performed at room temperature and conducted by connecting the *p*-H_2 source to a bubbling SABRE setup via PTFE tubing, with *p*-H_2 flow controlled by a mass-flow controller. For MRI experiments (unless stated otherwise), *p*-H_2 was bubbled through a 0.6 mL solution composed of 100 mM substrate (Py or nico) dissolved in CD_3OD with 5.7 mM Ir(IMes)(COD)Cl precatalyst (reaction scheme depicted in Figure 2), located in a 5 mm

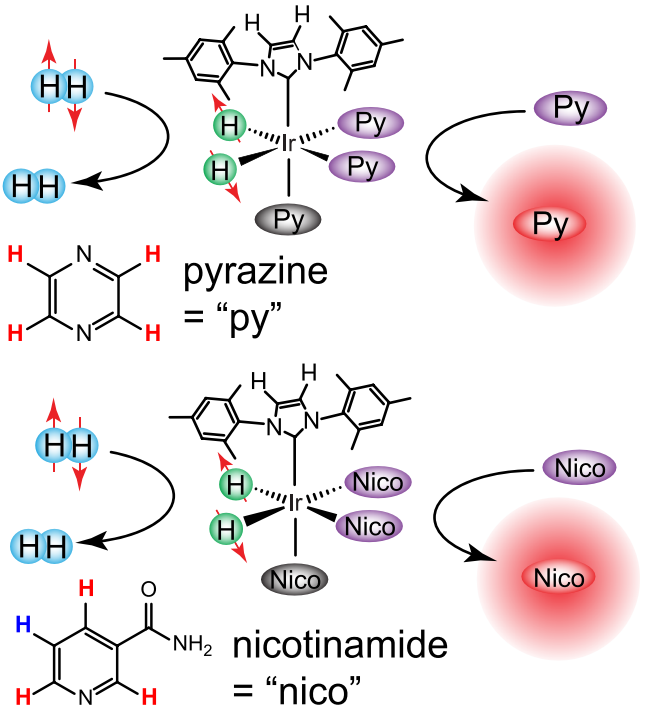

Figure 2. Structures and reaction schemes for SABRE using the IrIMes catalyst to transfer nuclear spin order from *p*-H_2-sourced hydrides (green) to transiently bound substrates (purple): (a) pyrazine ("Py") and (b) nicotinamide ("nico"), resulting in free HP substrates (red). Dissolved H_2 gas is shown in light blue; red arrows represent the nuclear spins—spin-paired for *p*-H_2 [upper-left of (a,b)]—whereas slanting of arrows represents the partial mixing of spin states during exchange, ultimately yielding "spent" H_2 gas.

NMR tube (length = 103.5 mm). The reduced height allowed the NMR tube to be placed vertically within the MRI scanner's head coil while connected to the PTFE umbilical tubing. Benchtop NMR required that the sample be placed in a standard-length 5 mm NMR tube.

Prior to SABRE experiments with a given sample, the precatalyst was activated by continuously bubbling *p*-H_2 for 20 min at 90 sccm. Next, initial ^{1}H SABRE was performed by bubbling for 30 s (90 sccm, ∼75 PSI overpressure) at ∼6 mT in the fringe field of the MRI magnet (or within the head coil at 64 mT), followed by rapid manual sample transfer to a benchtop NMR spectrometer (Nanalysis 60Pro). This spectrometer was used both to confirm catalyst activation and SABRE activity and to perform SABRE quantification at 1.4 T. For imaging experiments, the sample was then transferred to the shortened NMR tube, reconnected to the umbilical, repressurized, and placed in the MRI scanner where SABRE was imaged in situ[14,15,28] at 64 mT (Hyperfine Inc., Guilford, "*Swoop*" Mk1.6 (software versions 8.5−8.7); Figure

https://doi.org/10.1021/acs.analchem.4c01299
Anal. Chem. 2024, 96, 10348−10355

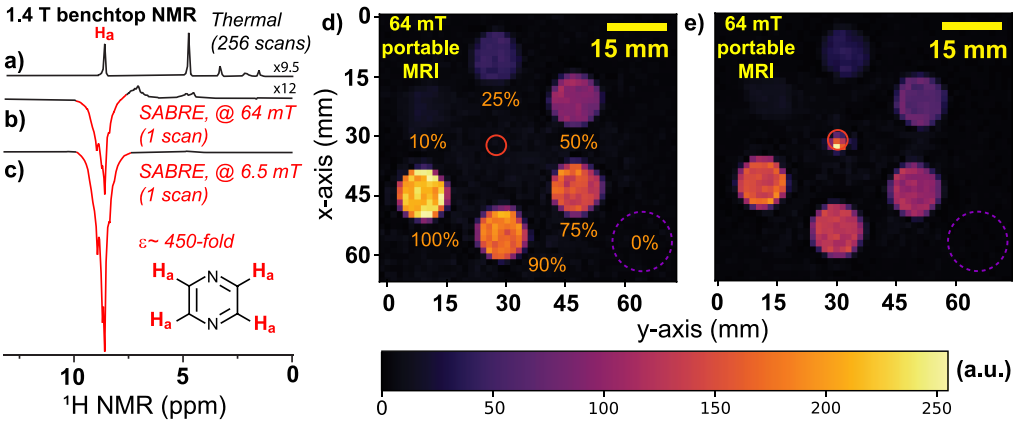

Figure 3. ^{1}H SABRE imaging of pyrazine using a 64 mT MRI scanner compared with NMR detection using a 1.4 T benchtop spectrometer. (a) Reference spectrum from a thermally polarized sample (100 mM Py, 5.7 mM catalyst in CD_3OD); the bubbling capillary tube was removed (to improve shim). (b,c) SABRE spectra with *p*-H_2 bubbling performed at 64 (b) or ∼6 mT (c) prior to sample transfer to 1.4 T for detection. Spectra in (a,b) are vertically scaled by 9.5- and 12-fold, respectively, compared to that in (c), where the Py SABRE enhancement was ∼450-fold at 1.4 T. (d) Selected 2D coronal "slice" from a 3D image of the seven water-filled falcon tubes and a NMR tube (position marked by the red circle) containing the same substances and concentrations as those in (a) within the head coil of the 64 mT MRI scanner—in the absence of *p*-H_2 bubbling. The image was obtained using a FSE sequence (AT: 5 min, 26 s; DR: 1.5 × 1.5 × 5 mm^3). The H_2O (versus D_2O) percentage is provided for each sample. The position of a "0%" H_2O/100% D_2O sample is indicated by the dashed purple circle. (e) Same as (d), but with continuous bubbling of *p*-H_2 (20 sccm), yielding strongly enhanced signals from the NMR tube. Image SNR for the SABRE-enhanced region was 110 (see Supporting Information for details).

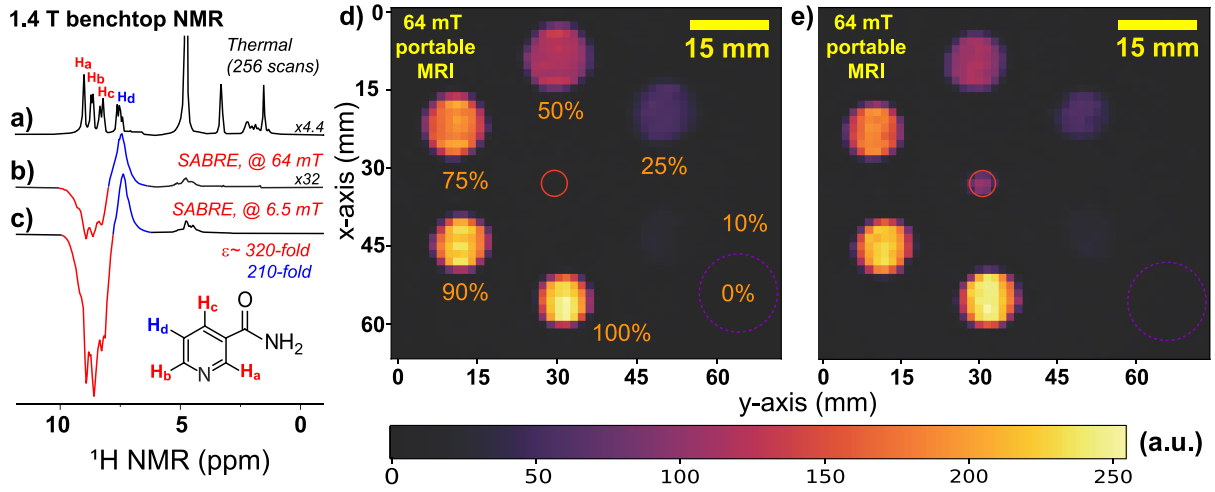

Figure 4. Same as Figure 3, except that the substrate was 100 mM nico. Note the mixed signs of the SABRE enhancements. Spectra in (a,b) are scaled by 32- and 4.4-fold, respectively, compared to that in (c), where the SABRE enhancements were ∼ (−)320-fold (H_a−H_c, red) and ∼(+)210-fold (H_d, blue), respectively, at 1.4 T. No signal is observed in the central NMR tube without *p*-H_2 bubbling (d). A SABRE-enhanced signal is observed with *p*-H_2 bubbling (e). Image SNR for the SABRE-enhanced region was 45.

1) with low-flow continuous *p*-H_2 bubbling (20 sccm, unless stated otherwise). LF scanners suffer much less from susceptibility distortion, enabling imaging during continuous gentle bubbling. 3D imaging was performed either with (1) a preloaded fast spin echo (FSE; i.e., "T_2 contrast") sequence [digital resolution (DR): 1.5 × 1.5 × 5 mm^3; field of view (FOV): 20 × 18 × 20 cm^3; acquisition time (AT): 5 min, 26 s]; or (2) a preloaded modified spin-density map (DR: 1 × 1 × 5 mm^3; FOV: 14 cm isotropic; AT: 15 s). For (2), images were not obtained with continuous *p*-H_2 bubbling (see below). Both RF broadcast and MRI detection were performed with the scanner's installed head coil (see Supporting Information for image processing and additional methods details).

RESULTS AND DISCUSSION

Py was chosen as the first molecule to be studied owing to its high molecular symmetry, which provides a simplified spectrum and a common SABRE efficiency for its four ^{1}H spins at a given magnetic field. Following 30 s of *p*-H_2 bubbling at ∼6 mT with a 100 mM Py sample, strong, inverted (emissive) signals were clearly observed from the aromatic region of the ^{1}H NMR spectra (e.g., Figure 3c—as expected for ^{1}H SABRE when performed near the ideal magnetic field[17]). Comparison with a corresponding reference spectrum obtained from a thermally polarized sample (e.g., Figure 3a) indicated enhancements of ∼450-fold for the Py ^{1}H resonance detected at 1.4 T.

Transfer of an identically prepared sample to a shortened 5 mm tube and connection to the *p*-H_2 line allowed placement in

https://doi.org/10.1021/acs.analchem.4c01299
Anal. Chem. 2024, 96, 10348−10355

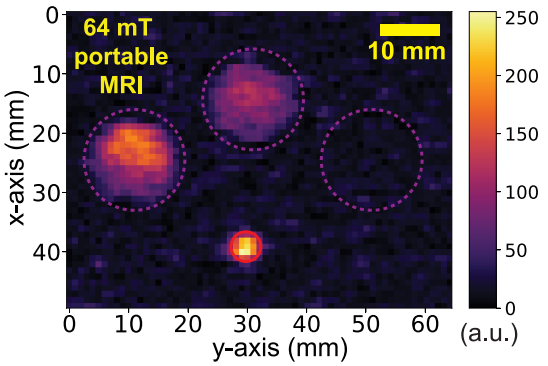

Figure 5. Selected 2D coronal "pseudoslice" from a 3D modified spin density MR image obtained from three of the water tubes (respectively containing 100%, 50%, and "0%" H_2O, backfilled with D_2O) and a NMR tube (outlined by the red circle) containing a 100 mM pyrazine sample, acquired following 30 s p-H_2 bubbling (90 sccm) near the optimal SABRE field (~6 mT) and rapid manual transfer of the sample to the scanner's head coil. Image SNR for the SABRE-enhanced region was 17. Digital resolution: 1 × 1 × 5 mm^3; acquisition time: 15 s.

the MRI scanner for SABRE imaging, along with the H_2O/D_2O calibration tubes. Using the FSE sequence, clear images are obtained for the H_2O/D_2O samples—with signal intensities corresponding to the ^1H concentration in each sample (Figure 3d). However, in the absence of p-H_2 bubbling, no signal is observed from the NMR tube.

Given that the T_1 of ^1H Py spins is much shorter than the FSE image acquisition time, it was necessary to attempt SABRE within the imaging field (64 mT)—an order of magnitude higher than the field at which most-efficient ^1H SABRE is expected.[17] Moreover, the p-H_2 flow rate was reduced to 20 sccm to mitigate disturbance of the liquid level within the tube. Nevertheless, despite such nonoptimal conditions, a strong signal is observed from the NMR tube with p-H_2 bubbling (Figure 3e)—roughly similar to that obtained with pure water. Given that SABRE was performed in a nonideal magnetic field and that there is almost no chemical-shift difference between the resonances in the sample at 64 mT, the image alone is insufficient to determine its chemical origin. For example, one might be concerned that the 64 mT MRI signal instead was originating from free HP orthohydrogen (o-H_2) or HP (bound) hydride spins.[15]

To investigate such possibilities further, SABRE was performed with p-H_2 bubbling at 64 mT but with rapid transfer to the benchtop NMR for detection (Figure 3b). Albeit significantly reduced in size compared to that in Figure

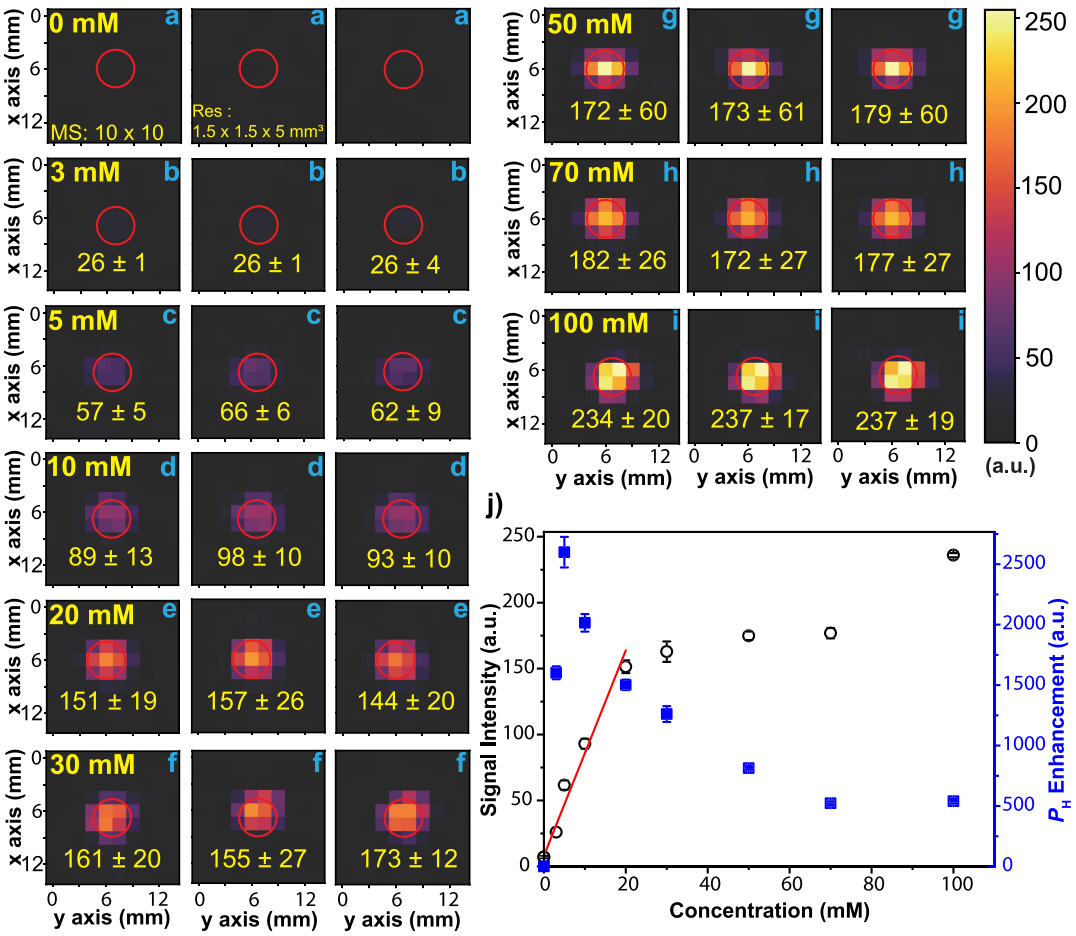

Figure 6. (a–i) Images obtained the same as in Figure 3, except with varying [Py] and a 10:1 substrate/catalyst ratio (performed in triplicate). Regions depicted show the positions of the SABRE NMR tube (outlined by red circles); the average signal and standard deviation from the tube region are reported in each image. (a) 0 mM Py; (b) 3 mM; (c) 5 mM; (d) 10 mM; (e) 20 mM; (f) 30 mM; (g) 50 mM; (h) 70 mM; (i) 100 mM. (j) Plots of average MRI signal (white circles) and P_H enhancement (blue squares) versus [Py], derived from the images in (a–i). Signal values from the lower concentrations were linearly fit (red line) to obtain LOD/LOQ values (see Supporting Information).

https://doi.org/10.1021/acs.analchem.4c01299
Anal. Chem. 2024, 96, 10348−10355

3c, the resulting ^{1}H NMR showed SABRE enhancement of the Py resonance (∼20-fold at 1.4 T). Moreover, no strong signals were observed for HP *o*-H_2 (∼4.6 ppm) or the hydride region [∼(−)23 ppm, see Supporting Information]. Thus, we conclude that the signal from the 5 mm sample (Figure 3e) is from SABRE-enhanced Py. This conclusion is also supported by the lack of signal in a control image using deuterated Py (not shown).

As mentioned, nico was chosen as the other molecule for this study because of its biological relevance, high tolerability, and potential use as a HP MRI contrast agent.[27−31] As was done with Py, the SABRE response with nico was first evaluated via benchtop NMR. Following bubbling at ∼6 mT, an average enhancement of up to (−)320-fold was observed in the resonances of free nico (100 mM) at 1.4 T (Figure 4c)—calculated via comparison with a thermally polarized sample (Figure 4a).

Placement of an identically prepared sample in the MRI scanner allowed imaging with nico in the same manner as that performed with Py (Figure 4d,e). As expected, no signal is observed from the nico sample in the absence of *p*-H_2 bubbling (Figure 4d). However, *p*-H_2 bubbling and reimaging allowed a signal to be observed from the central NMR tube—ostensibly from SABRE-hyperpolarized nico (Figure 4e). This *p*-H_2-enhanced MRI signal was clearly weaker than that from HP Py (Figure 3e).

Although this observation of a weaker HP MRI signal can be partially explained by the intrinsically lower enhancement observed for nico versus Py (cf. Figures 3c and 4c), there is likely an additional contribution. Nico, unlike Py, has several nonequivalent ^{1}H resonances. The small residual frequency dispersion among these resonances, even at such LFs, can yield qualitative differences in SABRE behavior—particularly when the mixing field is changed. For example, the spectrum in Figure 4c shows a significant positively phased SABRE enhancement (∼210-fold) for the H_d resonance at 1.4 T following SABRE at ∼6 mT, likely reflecting a nonoptimal SABRE mixing field. However, this absorptive component is dwarfed by the emissive resonances assigned collectively to H_a−H_c. But when SABRE is performed at the MRI scanner field of 64 mT (Figure 4b), not only is the overall total signal detected at 1.4 T greatly reduced but the absorptive and emissive components are now much closer in size (cf. Figure 3b,c). Thus, when a nico sample is imaged at 64 mT, the collapse in chemical shift dispersion at the lower field should cause the positively and negatively enhanced resonances to overlap, resulting in partial cancellation of the SABRE effect in the nico image (Figure 4e; note that the scanner's imaging data is not phase-sensitive).

Figures 3 and 4 clearly show successful SABRE-enhanced imaging with the 64 mT scanner using both substrates. We next investigated to see if a calibration protocol could be developed using H_2O/D_2O reference samples of varying ratios that could be used to reliably quantify the SABRE MRI enhancement. Toward that end, the average signal from each H_2O/D_2O falcon tube was determined for each image and plotted against the ^{1}H concentrations (see Supporting Information for details and graphs). As examples, the signals from the images in Figures 3e and 4e were well-reproduced by linear fits. These well-behaved responses and knowledge of the relevant ^{1}H concentrations in all samples allowed facile quantification of the SABRE enhancements, yielding values of ∼310-fold and ∼160-fold for Py and nico, respectively (see Supporting Information).

One should remember that the NMR/MRI signal enhancement provided by hyperpolarization is inversely proportional to the magnetic field, here differing by a factor of 1.4 T/0.064 T = 21.9-fold for the two fields used. Thus, to directly compare the enhancements for Py obtained at these two fields, one needs to divide the 0.064 T enhancement by 21.9. In other words, the nuclear spin polarization values achieved in the MRI scanner are much lower than those reported for the benchtop NMR spectrometer when SABRE was performed at the optimal field of ∼6 mT (as expected). The field-normalized enhancement measured for the 64 mT image is much closer, ∼1.4-fold lower than that obtained at 1.4 T with the same 64 mT mixing field. The field-normalized enhancement for nico is likely further reduced by the frequency overlap of positively and negatively enhanced resonances, as explained above.

Particularly given the long scan times (relative to T_1) of the 3D pulse sequences utilized above, achieving quantifiable SABRE enhancement on this scanner benefited from continuous *p*-H_2 bubbling and SABRE hyperpolarization throughout each scan. Indeed, while both SABRE and its sister technique, hydrogenative parahydrogen-induced polarization (PHIP),[11,12,37] have been used for LF NMR and MRI studies (e.g., refs 9 and 13−16), SABRE does not involve the irreversible chemical change of the substrate. Thus, SABRE can be performed continuously on the same sample for extended periods of time. This feature is useful for many LF applications (e.g., ref 20) and greatly facilitates MR technique development. However, if bolus production of a SABRE-hyperpolarized agent is to be used (e.g., to benefit from more-efficient hyperpolarization conditions), then much faster scanning must be achieved in order to compete with rapid hyperpolarization decay from T_1 relaxation. On the other hand, the enormous signal enhancement provided by hyperpolarization can enable ultrafast (even subsecond 3D) MRI,[14,15,38−40] limited only by the technical capabilities of the scanner.

Thus, we also investigated the potential for using "fast" 3D scanning for obtaining improved SABRE imaging on this device. For these experiments, SABRE was first performed by bubbling *p*-H_2 at 90 sccm in the scanner's fringe field at ∼6 mT for 30 s, followed by rapid transfer to the head coil prior to scanning with a modified spin density map sequence. Using a smaller FOV ($0.14 \times 0.14 \times 0.14$ m^3) allowed full 3D read-out in 15 s—within $\sim 2T_1$ of the Py ^{1}H spins—but also with improved digital resolution ($1.0 \times 1.0 \times 5$ mm^3). Although the signals from the water tubes were weak, a bright signal was observed from hyperpolarized Py (Figure 5). The signals from each tube were plotted against the ^{1}H concentration (see Supporting Information), and the resulting linear fit indicated an enhancement of ∼590-fold at 64 mT. This ∼2-fold improvement in the SABRE enhancement compared to that in Figure 3e (∼310-fold) showed that the use of the improved SABRE conditions more than compensated for the polarization losses suffered by relaxation and the lack of continuously generated ^{1}H magnetization.

Finally, although the above technique-development experiments used 100 mM substrates, imaging with much lower concentrations is also possible. We performed a series of SABRE imaging experiments with varying Py concentrations and a fixed 10:1 substrate/catalyst ratio, allowing LOD and LOQ to be determined. Otherwise, using the same conditions as those in Figure 3, we found we could readily image SABRE

https://doi.org/10.1021/acs.analchem.4c01299
Anal. Chem. 2024, 96, 10348−10355

down to 3−5 mM substrates (Figure 6). Initially, the signal is not reduced linearly with decreasing concentration because the SABRE efficiency (and hence polarization) tends to increase with a lower substrate concentration until ultimately reaching a quasi-linear dependence (Figure 6j—see also Supporting Information). Thus, the lower concentration points were fit linearly to determine LOD and LOQ: 3.3 and 10.1 mM, respectively (see Supporting Information). Moreover, given that the average ^{1}H enhancement for these lower concentrations was ∼1900-fold [with ^{1}H polarization (P_H) of "only" ∼0.04%], a P_H of 1% should yield a corresponding >20-fold improvement in LOD/LOQ. Such a P_H value is routinely achievable under more favorable conditions.[34]

Our studies clearly demonstrate the feasibility of molecular imaging using ^{1}H detection of HP media at relatively low product of polarization and concentration (0.13%·mM). A wide range of HP contrast agents readily surpass this limit under biomedically relevant conditions. For example, the corresponding metric is over 10%·mM for ^{1}H-hyperpolarized propane and diethyl ether gases (e.g., ref 41), indicating that ventilation imaging using these types of inhalable contrast agents is certainly feasible using such a bed-side MRI scanner platform. Moreover, injectable hyperpolarized [1-^{13}C]pyruvate and its metabolic product [1-^{13}C]lactate are estimated to exceed 1%·mM for *Pc* in tumors (where the lactate concentration reaches up to 30 mM[42]) and other tissues metabolically altered by disease. A number of ^{1}H-detection schemes of HP [1-^{13}C]pyruvate and [1-^{13}C]lactate have been demonstrated in vivo,[43] indicating that molecular imaging of pyruvate is well within reach of the sensitivity of this LF MRI scanner. Indeed, more recent development of ^{1}H-only approaches for sensing of pyruvate and its metabolic product lactate[44,45] raises an intriguing possibility of efficient molecular imaging of HP pyruvate metabolism in this scanner. We envision the near-future utility of such approaches for imaging of brain function and applications related to brain cancer and neurodegeneration.

CONCLUSIONS

We have reported on initial efforts to integrate SABRE hyperpolarization and imaging with a portable, point-of-care clinical MRI scanner. Enhanced MRI with two substrates, pyrazine and nicotinamide, was demonstrated and compared with benchtop NMR. The use of phantoms containing varying quantities of H versus D spins enabled the development of a simple approach to quantify SABRE enhancements. Although maximizing SABRE was not the primary point of the present work, enhancements up to ∼590-fold were observed in the resulting images with 100 mM substrates. Up to ∼2600-fold enhancements were obtained at lower concentrations, allowing few-mM substrate concentrations to be imaged and pointing the way to future gains. Ongoing efforts to improve on these results include the following: optimization of the MRI sequences for faster SABRE imaging; integration with a continuous recirculation setup (e.g., refs 20, 26, and 46−48) to enable SABRE at optimal fields and continuous resupply of HP liquids to the scanner; and scaling up HP agent production to allow SABRE imaging of larger objects. The present work, along with recent efforts toward the preparation of biocompatible solutions with SABRE-hyperpolarized agents[49−51] and the first demonstrations of in vivo SABRE imaging,[52,53] bode well for future preclinical and clinical SABRE-enhanced MRI with LF point-of-care scanners for envisioned biomedical applications. Indeed, although the present scanner can only detect protons, the recent realization of proton-only detection of HP heteronuclei[44,45,54] opens the possibility of point-of-care molecular imaging of HP ^{13}C-based metabolic agents like HP pyruvate, the subject of 30-plus clinical trials to date.

ASSOCIATED CONTENT

Supporting Information

The Supporting Information is available free of charge at https://pubs.acs.org/doi/10.1021/acs.analchem.4c01299.

Image-processing protocols, calculations of SABRE enhancements, and additional experimental data and methods details (PDF)

AUTHOR INFORMATION

Corresponding Author

Boyd M. Goodson − *School of Chemical and Biomolecular Sciences, Southern Illinois University, Carbondale, Illinois 62901, United States;* orcid.org/0000-0001-6079-5077; Email: bgoodson@chem.siu.edu

Authors

Nadiya Iqbal − *School of Chemical and Biomolecular Sciences, Southern Illinois University, Carbondale, Illinois 62901, United States*

Drew O. Brittin − *School of Chemical and Biomolecular Sciences, Southern Illinois University, Carbondale, Illinois 62901, United States*

Praveen J. Daluwathumullagamage − *School of Chemical and Biomolecular Sciences, Southern Illinois University, Carbondale, Illinois 62901, United States*

Md Shahabuddin Alam − *School of Chemical and Biomolecular Sciences, Southern Illinois University, Carbondale, Illinois 62901, United States*

Ishani M. Senanayake − *School of Chemical and Biomolecular Sciences, Southern Illinois University, Carbondale, Illinois 62901, United States*

A. Tobi Gafar − *School of Chemical and Biomolecular Sciences, Southern Illinois University, Carbondale, Illinois 62901, United States*

Zahid Siraj − *School of Chemical and Biomolecular Sciences, Southern Illinois University, Carbondale, Illinois 62901, United States*

Anthony Petrilla − *School of Chemical and Biomolecular Sciences, Southern Illinois University, Carbondale, Illinois 62901, United States*

Margaret Pugh − *School of Chemical and Biomolecular Sciences, Southern Illinois University, Carbondale, Illinois 62901, United States*

Brockton Tonazzi − *School of Medicine, Southern Illinois University, Carbondale, Illinois 62901, United States*

Sudarshan Ragunathan − *Hyperfine Inc., Guilford, Connecticut 06437, United States*

Megan E. Poorman − *Hyperfine Inc., Guilford, Connecticut 06437, United States*

Laura Sacolick − *Hyperfine Inc., Guilford, Connecticut 06437, United States*

Thomas Theis − *Department of Chemistry, North Carolina State University, Raleigh, North Carolina 27695, United States;* orcid.org/0000-0001-6779-9978

Matthew S. Rosen − *A.A. Martinos Center for Biomedical Imaging, Massachusetts General Hospital and Harvard Medical School, Boston, Massachusetts 02129, United States*
Eduard Y. Chekmenev − *Department of Chemistry, Integrative Biosciences (IBio), Karmanos Cancer Institute (KCI), Wayne State University, Detroit, Michigan 48202, United States;* orcid.org/0000-0002-8745-8801

Complete contact information is available at: https://pubs.acs.org/10.1021/acs.analchem.4c01299

Notes

The authors declare the following competing financial interest(s): M.S.R. is a founder and equity holder of Hyperfine, Inc. T.T. and M.S.R. are cofounders and equity holders of Vizma Life Sciences (VLS). The terms of T.T.'s arrangement have been reviewed and approved by NC State University in accordance with its policy on objectivity in research. E.Y.C. serves on the Scientific Advisory Board (SAB) of VLS. E.Y.C. and B.M.G. declare stake of ownership of XeUS Technologies Ltd.

■ ACKNOWLEDGMENTS

We thank P. Tomhon (NCSU) for helpful discussions. Funding: DOD CDMRP (W81XWH-20-10578 and W81XWH-20-10576), NSF (CHE-1905341 and 1904780 and REU DMR-2150489), and NIH (R01EB029829, R01EB034197, R21HL154032, and R21EB033872). M.S.R. acknowledges the generous support of the Kiyomi and Ed Baird MGH Research Scholar program.

■ REFERENCES

(1) Arnold, T. C.; Freeman, C. W.; Litt, B.; Stein, J. M. *J. Magn. Reson. Imaging* **2023**, *57*, 25−44.
(2) Kimberly, W. T.; Sorby-Adams, A. J.; Webb, A. G.; Wu, E. X.; Beekman, R.; Bowry, R.; Schiff, S. J.; de Havenon, A.; Shen, F. X.; Sze, G.; Schaefer, P.; Iglesias, J. E.; Rosen, M. S.; Sheth, K. N. *Nat. Rev. Bioeng.* **2023**, *1*, 617−630.
(3) de Havenon, A.; Parasuram, N. R.; Crawford, A. L.; Mazurek, M. H.; Chavva, I. R.; Yadlapalli, V.; Iglesias, J. E.; Rosen, M. S.; Falcone, G. J.; Payabvash, S.; Sze, G.; Sharma, R.; Schiff, S. J.; Safdar, B.; Wira, C.; et al. *J. Am. Heart Assoc.* **2023**, *12*, No. e029242.
(4) Sujijantarat, N.; Koo, A. B.; Jambor, I.; Malhotra, A.; Mazurek, M. H.; Parasuram, N.; Yadlapalli, V.; Chavva, I. R.; Lalwani, D.; Zabinska, J.; Roy, J. M.; Antonios, J. P.; Elsamadicy, A. A.; Renedo, D.; Hebert, R. M.; et al. *Stroke Vasc. Neurol.* **2023**, 3, No. e000921.
(5) Sheth, K. N.; Yuen, M. M.; Mazurek, M. H.; Cahn, B. A.; Prabhat, A. M.; Salehi, S.; Shah, J. T.; By, S.; Welch, E. B.; Sofka, M.; Sacolick, L. I.; Kim, J. A.; Payabvash, S.; Falcone, G. J.; Gilmore, E. J.; et al. *Sci. Rep.* **2022**, *12*, 67.
(6) Yuen, M. M.; Prabhat, A. M.; Mazurek, M. H.; Chavva, I. R.; Crawford, A.; Cahn, B. A.; Beekman, R.; Kim, J. A.; Gobeske, K. T.; Petersen, N. H.; Falcone, G. J.; Gilmore, E. J.; Hwang, D. Y.; Jasne, A. S.; Amin, H.; et al. *Sci. Adv.* **2022**, *8*, No. eabm3952.
(7) Iglesias, J. E.; Schleicher, R.; Laguna, S.; Billot, B.; Schaefer, P.; McKaig, B.; Goldstein, J. N.; Sheth, K. N.; Rosen, M. S.; Kimberly, W. T. *Radiology* **2023**, *306*, No. e220522.
(8) Sheth, K. N.; Mazurek, M. H.; Yuen, M. M.; Cahn, B. A.; Shah, J. T.; Ward, A.; Kim, J. A.; Gilmore, E. J.; Falcone, G. J.; Petersen, N.; Gobeske, K. T.; Kaddouh, F.; Hwang, D. Y.; Schindler, J.; Sansing, L.; et al. *JAMA Neurol.* **2021**, *78*, 41−47.
(9) Blanchard, J. W.; Budker, D.; Trabesinger, A. *J. Magn. Reson.* **2021**, *323*, 106886.
(10) Bagnall, G. C.; Koonjoo, N.; Altobelli, S. A.; Conradi, M. S.; Fukushima, E.; Kuethe, D. O.; Mullet, J. E.; Neely, H.; Rooney, W. L.; Stupic, K. F.; Weers, B.; Zhu, B.; Rosen, M. S.; Morgan, C. L. S. *Geoderma* **2020**, *370*, 114356.
(11) Nikolaou, P.; Goodson, B. M.; Chekmenev, E. Y. *Chem.—Eur. J.* **2015**, *21*, 3156−3166.
(12) Eills, J.; Budker, D.; Cavagnero, S.; Chekmenev, E. Y.; Elliott, S. J.; Jannin, S.; Lesage, A.; Matysik, J.; Meersmann, T.; Prisner, T.; Reimer, J. A.; Yang, H.; Koptyug, I. V. *Chem. Rev.* **2023**, *123*, 1417−1551.
(13) Coffey, A. M.; Truong, M. L.; Chekmenev, E. Y. *J. Magn. Reson.* **2013**, *237*, 169−174.
(14) Coffey, A. M.; Kovtunov, K. V.; Barskiy, D. A.; Koptyug, I. V.; Shchepin, R. V.; Waddell, K. W.; He, P.; Groome, K. A.; Best, Q. A.; Shi, F.; Goodson, B. M.; Chekmenev, E. Y. *Anal. Chem.* **2014**, *86*, 9042−9049.
(15) Barskiy, D. A.; Kovtunov, K. V.; Koptyug, I. V.; He, P.; Groome, K. A.; Best, Q. A.; Shi, F.; Goodson, B. M.; Shchepin, R. V.; Truong, M. L.; Coffey, A. M.; Waddell, K. W.; Chekmenev, E. Y. *ChemPhysChem* **2014**, *15*, 4100−4107.
(16) Lehmkuhl, S.; Suefke, M.; Kentner, A.; Yen, Y.-F.; Blümich, B.; Rosen, M. S.; Appelt, S.; Theis, T. *J. Chem. Phys.* **2020**, *152*, 184202.
(17) Adams, R. W.; Aguilar, J. A.; Atkinson, K. D.; Cowley, M. J.; Elliott, P. I.; Duckett, S. B.; Green, G. G.; Khazal, I. G.; López-Serrano, J.; Williamson, D. C. *Science* **2009**, *323*, 1708−1711.
(18) Theis, T.; Ledbetter, M. P.; Kervern, G.; Blanchard, J. W.; Ganssle, P. J.; Butler, M. C.; Shin, H. D.; Budker, D.; Pines, A. *J. Am. Chem. Soc.* **2012**, *134*, 3987−3990.
(19) Glöggler, S.; Muller, R.; Colell, J.; Emondts, M.; Dabrowski, M.; Blumich, B.; Appelt, S. *Phys. Chem. Chem. Phys.* **2011**, *13*, 13759−13764.
(20) Blanchard, J. W.; Ripka, B.; Suslick, B. A.; Gelevski, D.; Wu, T.; Munnemann, K.; Barskiy, D. A.; Budker, D. *Magn. Reson. Chem.* **2021**, *59*, 1208−1215.
(21) Pham, P.; Hilty, C. *Chem. Sci.* **2023**, *14*, 10258−10263.
(22) Sheth, K.; Cahn, B.; Salehi, S.; Shah, J.; By, S.; Welch, E. B.; Sofka, M.; Sacolick, L.; Yuen, M.; Mazurek, M.; et al. *Neurology* **2020**, *94*, 2771.
(23) Mazurek, M. H.; Cahn, B.; Yuen, M. M.; Prabhat, A. M.; Chavva, I. R.; Shah, J. T.; Crawford, A. L.; Welch, E. B.; Rothberg, J.; Sacolick, L.; Poole, M.; Wira, C.; Matouk, C. C.; Ward, A.; Timario, N.; et al. *Nat. Commun.* **2021**, *12*, 5119.
(24) Jordanova, K. V.; Martin, M. N.; Ogier, S. E.; Poorman, M. E.; Keenan, K. E. *Magn. Reson. Mater. Phys.* **2023**, *36*, 487−498.
(25) Oberdick, S. D.; Jordanova, K. V.; Lundstrom, J. T.; Parigi, G.; Poorman, M. E.; Zabow, G.; Keenan, K. E. *Sci. Rep.* **2023**, *13*, 11520.
(26) TomHon, P. M.; Han, S.; Lehmkuhl, S.; Appelt, S.; Chekmenev, E. Y.; Abolhasani, M.; Theis, T. *ChemPhysChem* **2021**, *22*, 2526−2534.
(27) Theis, T.; Truong, M. L.; Coffey, A. M.; Shchepin, R. V.; Waddell, K. W.; Shi, F.; Goodson, B. M.; Warren, W. S.; Chekmenev, E. Y. *J. Am. Chem. Soc.* **2015**, *137*, 1404−1407.
(28) Kovtunov, K. V.; Kidd, B. E.; Salnikov, O. G.; Bales, L. B.; Gemeinhardt, M. E.; Gesiorski, J.; Shchepin, R. V.; Chekmenev, E. Y.; Goodson, B. M.; Koptyug, I. V. *J. Phys. Chem. C* **2017**, *121*, 25994−25999.
(29) Hövener, J. B.; Schwaderlapp, N.; Borowiak, R.; Lickert, T.; Duckett, S. B.; Mewis, R. E.; Adams, R. W.; Burns, M. J.; Highton, L. A. R.; Green, G. G. R.; Olaru, A. M.; Hennig, J.; von Elverfeldt, D. *Anal. Chem.* **2014**, *86*, 1767−1774.
(30) Linnik, I. V.; Rayner, P. J.; Stow, R. A.; Duckett, S. B.; Cheetham, G. M. *Eur. J. Pharm. Sci.* **2019**, *135*, 32−37.
(31) Peters, J. P.; Brahms, A.; Janicaud, V.; Anikeeva, M.; Peschke, E.; Ellermann, F.; Ferrari, A.; Hellmold, D.; Held-Feindt, J.; Kim, N. m.; Meiser, J.; Aden, K.; Herges, R.; Hövener, J. B.; Pravdivtsev, A. N.; et al. *Sci. Adv.* **2023**, *9*, No. eadd3643.
(32) Vázquez-Serrano, L. D.; Owens, B. T.; Buriak, J. M. *Chem. Commun.* **2002**, 2518−2519.
(33) Torres, O.; Martin, M.; Sola, E. *Organometallics* **2009**, *28*, 863−870.

(34) Cowley, M. J.; Adams, R. W.; Atkinson, K. D.; Cockett, M. C.; Duckett, S. B.; Green, G. G.; Lohman, J. A.; Kerssebaum, R.; Kilgour, D.; Mewis, R. E. *J. Am. Chem. Soc.* **2011**, *133*, 6134−6137.
(35) Alam, M. S.; Li, X.; Brittin, D. O.; Islam, S.; Deria, P.; Chekmenev, E. Y.; Goodson, B. M. *Angew. Chem., Int. Ed.* **2023**, *62*, No. e202213581.
(36) Birchall, J. R.; Coffey, A. M.; Goodson, B. M.; Chekmenev, E. Y. *Anal. Chem.* **2020**, *92*, 15280−15284.
(37) Bowers, C. R.; Weitekamp, D. P. *J. Am. Chem. Soc.* **1987**, *109*, 5541−5542.
(38) Bhattacharya, P.; Harris, K.; Lin, A.; Mansson, M.; Norton, V. A.; Perman, W.; Weitekamp, D. P.; Ross, B. D. *Magn. Reson. Mater. Phys.* **2005**, *18*, 245−256.
(39) Hövener, J. B.; Schwaderlapp, N.; Lickert, T.; Duckett, S. B.; Mewis, R. E.; Highton, L. A.; Kenny, S. M.; Green, G. G. R.; Leibfritz, D.; Korvink, J. G.; Hennig, J.; von Elverfeldt, D. *Nat. Commun.* **2013**, *4*, 2946.
(40) Kovtunov, K. V.; Romanov, A. S.; Salnikov, O. G.; Barskiy, D. A.; Chekmenev, E. Y.; Koptyug, I. V. *Tomography* **2016**, *2*, 49−55.
(41) Ariyasingha, N. M.; Chowdhury, M. R. H.; Samoilenko, A.; Salnikov, O. G.; Chukanov, N. V.; Kovtunova, L. M.; Bukhtiyarov, V. I.; Shi, Z.; Luo, K.; Tan, S.; Koptyug, I. V.; Goodson, B. M.; Chekmenev, E. Y. *Chem.—Eur. J.* **2024**, *30*, No. e202304071.
(42) de la Cruz-López, K. G.; Castro-Muñoz, L. J.; Reyes-Hernández, D. O.; García-Carrancá, A.; Manzo-Merino, J. *Front. Oncol.* **2019**, *9*, 1143.
(43) Wang, J.; Kreis, F.; Wright, A. J.; Hesketh, R. L.; Levitt, M. H.; Brindle, K. M. *Magn. Reson. Med.* **2018**, *79*, 741−747.
(44) Mandzhieva, I.; Adelabu, I.; Chekmenev, E. Y.; Theis, T. *ACS Sens.* **2022**, *7*, 3773−3781.
(45) Mandzhieva, I.; Adelabu, I.; Nantogma, S.; Chekmenev, E. Y.; Theis, T. *ACS Sens.* **2023**, *8*, 4101−4110.
(46) Zhao, T. Y.; Lapak, M. P.; Behera, R.; Zhao, H.; Ferrer, M.-J.; Weaver, H. E. H.; Huang, W.; Bowers, C. R. *J. Magn. Reson. Open* **2022**, *12*−*13*, 100076.
(47) Lehmkuhl, S.; Wiese, M.; Schubert, L.; Held, M.; Küppers, M.; Wessling, M.; Blümich, B. *J. Magn. Reson.* **2018**, *291*, 8−13.
(48) Štěpánek, P.; Sanchez-Perez, C.; Telkki, V.-V.; Zhivonitko, V. V.; Kantola, A. M. *J. Magn. Reson.* **2019**, *300*, 8−17.
(49) Barskiy, D. A.; Ke, L. A.; Li, X.; Stevenson, V.; Widarman, N.; Zhang, H.; Truxal, A.; Pines, A. *J. Phys. Chem. Lett.* **2018**, *9*, 2721−2724.
(50) Manoharan, A.; Rayner, P. J.; Iali, W.; Burns, M. J.; Perry, V. H.; Duckett, S. B. *ChemMedChem* **2018**, *13*, 352−359.
(51) Schmidt, A. B.; de Maissin, H.; Adelabu, I.; Nantogma, S.; Ettedgui, J.; TomHon, P.; Goodson, B. M.; Theis, T.; Chekmenev, E. Y. *ACS Sens.* **2022**, *7*, 3430−3439.
(52) MacCulloch, K.; Browning, A.; Guarin Bedoya, D. O.; McBride, S. J.; Abdulmojeed, M. B.; Dedesma, C.; Goodson, B. M.; Rosen, M. S.; Chekmenev, E. Y.; Yen, Y.-F.; TomHon, P.; Theis, T. *J. Magn. Reson. Open* **2023**, *16*−*17*, 100129.
(53) de Maissin, H.; Groß, P. R.; Mohiuddin, O.; Weigt, M.; Nagel, L.; Herzog, M.; Wang, Z.; Willing, R.; Reichardt, W.; Pichotka, M.; Heß, L.; Reinheckel, T.; Jessen, H. J.; Zeiser, R.; Bock, M.; et al. *Angew. Chem., Int. Ed.* **2023**, *62*, No. e202306654.
(54) Feng, Y.; Theis, T.; Liang, X.; Wang, Q.; Zhou, P.; Warren, W. S. *J. Am. Chem. Soc.* **2013**, *135*, 9632−9635.

https://doi.org/10.1021/acs.analchem.4c01299
Anal. Chem. 2024, 96, 10348−10355